Neurophotonics

Neurophotonics.SPIEDigitalLibrary.org

Fluorescence micro-optical sectioning tomography using acousto-optical deflector-based confocal scheme

Xiaoli Qi
Tao Yang
Longhui Li
Jiancun Wang
Shaoqun Zeng
Xiaohua Lv

SPIE.

Neurophotonics 2(4), 041406 (Oct–Dec 2015)

Fluorescence micro-optical sectioning tomography using acousto-optical deflector-based confocal scheme

Xiaoli Qi,[a,b] Tao Yang,[a,b] Longhui Li,[a,b] Jiancun Wang,[a,b] Shaoqun Zeng,[a,b] and Xiaohua Lv[a,b,*]
[a]Britton Chance Center for Biomedical Photonics, Huazhong University of Science and Technology, Wuhan National Laboratory for Optoelectronics, 1037 Luoyu Road, Wuhan 430074, China
[b]Huazhong University of Science and Technology, Department of Biomedical Engineering, Key Laboratory of Biomedical Photonics of Ministry of Education, 1037 Luoyu Road, Wuhan 430074, China

Abstract. Fluorescent labeling has opened up the possibility of clarifying the complex distribution and circuit wiring of specific neural circuits for particular functions. To acquire the brain-wide fluorescently labeled neural wiring, we have previously developed the fluorescence micro-optical sectioning tomography imaging system. This employs simultaneous mechanical sectioning and confocal imaging of the slices, and is capable of acquiring the image dataset of a centimeter-sized whole-mouse brain at a voxel resolution of 1 μm. We analyze the key optical considerations for the use of an acousto-optical deflector (AOD) scanner-based confocal detection scheme in this system. As a result, the influence of confocal detection, the imaging site during sectioning, and AOD fast scan mode on signal-to-background noise ratio are described. It is shown that mechanical sectioning to separate the slice and optical sectioning by confocal detection should be combined to maximize background suppression in simultaneous fast scan imaging while sectioning system setup. [DOI: 10.1117/1.NPh.2.4.041406]

Keywords: brain-wide imaging; fluorescence microscopy; confocal imaging; acousto-optical deflector.

Paper 15020PSSRR received Apr. 25, 2015; accepted for publication Sep. 9, 2015; published online Oct. 15, 2015.

1 Introduction

Neural circuits are the internal structure and function basis for understanding the functions and diseases of the brain.[1,2] Many imaging methods have been developed to understand different aspects of the brain and its internal circuits at different spatial scales. Of the current brain imaging methods, magnetic resonance imaging (MRI) can provide whole-brain imaging to observe brain regions and their possible connections. However, the spatial resolution of MRI is not sufficient to resolve single neurons with their neurites, which have diameters ranging from submicron to a few microns.[3] Electron microscopes have been used to image the structure of synapses at nanometer resolution. However, imaging the whole mammalian brain with an electron microscope poses a great challenge in terms of imaging time and data storage. Hence, electron microscopes have only been used for the dissection of local neural circuits spanning millimeter-sized samples or small invertebrate brains.[4] At present, they are an impractical choice for understanding the long-range neural connections across a whole mammal brain.

Optical imaging can achieve submicron resolution,[5] which is suitable for resolving the neurites that form the projections and interconnections of neural wiring. The main limitation lies in the optical penetration depth, meaning that new imaging methods are required to image centimeter-sized brain samples with optical microscopy.[6] Confocal imaging has a penetration depth of less than 200 μm, and two-photon microscopy can penetrate to about 600 to 800 μm.[7] Light sheet microscopy uses chemically cleared "transparent" mouse brains and can penetrate relatively deep, albeit with some trade-off in terms of imaging quality at greater depth.[8] Mechanically slicing the specimen into thin sections before imaging is another way to circumvent the problem of limited imaging depth. With a section thickness of 50 nm, a much higher axial resolution can be achieved.[9] The knife-edge imaging method,[10] which employs simultaneous sectioning and imaging strategies, provides submicron three-dimensional (3-D) resolution over a large volume at an improved speed. We have previously developed a micro-optical sectioning tomography (MOST) technique. MOST combines microscopic imaging with automatic microtome slicing of the sample, and has been used to acquire 3-D structural datasets of Golgi-stained or Nissl-stained whole mouse brains.[11] Golgi staining can be used for neuronal morphology studies, whereas Nissl staining enables the somas of neurons to be located. However, these staining techniques do not have the function or cell-type specificity required to explore the wiring network of specific neural circuits.

Rapid developments in fluorescent proteins and molecular genetics enable the application of fluorescent labeling for targeting specific brain circuits. Using various labeling and genetic manipulation methods, genetically targeted and functionally related specific neural circuits can be identified by the expression of fluorescent proteins.[12–16] Brain-wide single neuron projections can also be targeted, and, with the help of trans-synaptic viral neuronal tracing, specific pathways connected to a single neuron or population of neurons at the virus injection site can be labeled.[17]

*Address all correspondence to: Xiaohua Lv, E-mail: xhlv@mail.hust.edu.cn

2329-423X/2015/$25.00

To map and visualize the fluorescently labeled neural circuits, we have developed a fluorescence micro-optical sectioning tomography system based on the MOST technique. This provides consistent micron-level resolution across a centimeter-sized, resin-embedded mouse brain, and has been used for the continuous tracing of brain-wide long-distance axonal projections.[18] In this paper, we discuss the technical details that enable fast and stable imaging with high signal-to-noise ratios (SNRs). The proposed system uses a confocal detection scheme with an acousto-optical deflector (AOD) as the scanner. We analyze and validate the effect of using confocal detection combined with mechanical sectioning on the imaging SNR. The use of a one-dimensional (1-D) AOD for fast scanning and the related astigmatism problem are also discussed.

2 System Setup

A schematic diagram of the fluorescence micro-optical sectioning tomography (fMOST) technique is shown in Fig. 1. The setup consists of a laser-scanning fluorescence microscope using an AOD scanner and a microtome, which works in a cycled imaging while sectioning mode. The excitation laser beam passes through a beam expander and an AOD scanner (DTSXY-A15-488, AA) performing y-axis scanning. The microscope light path contains a scan lens (L1, $f = 400$ mm), a tube lens (L2, $f = 180$ mm), and an objective (LUMPFLN $40\times/0.8$, Olympus). A resin-embedded brain sample is moved along the x-axis of a 3-D precision motorized stage (Aerotech) and sliced by a diamond knife (Diatome). Slicing and scan imaging occur at the same time; that is, the sliced sample is imaged while it is sliding over the diamond knife. The excited fluorescence is collected using the same objective, and is then passed through the tube lens, a dichroic mirror (Di01-R514-25×36, Semrock), and an emission filter (FF01-515/LP-25, Semrock) before being detected using a photomultiplier tube (PMT, R1924A, Hamamatsu). A custom-made slit (width = 50 μm) is placed in front of the PMT, located at the conjugate position of the focal plane of the objective. This is used to suppress background fluorescence. Data are acquired with a high-speed digitizer (PXI-5122, National Instruments). The pixel dwell time is 0.4 μs/pixel.

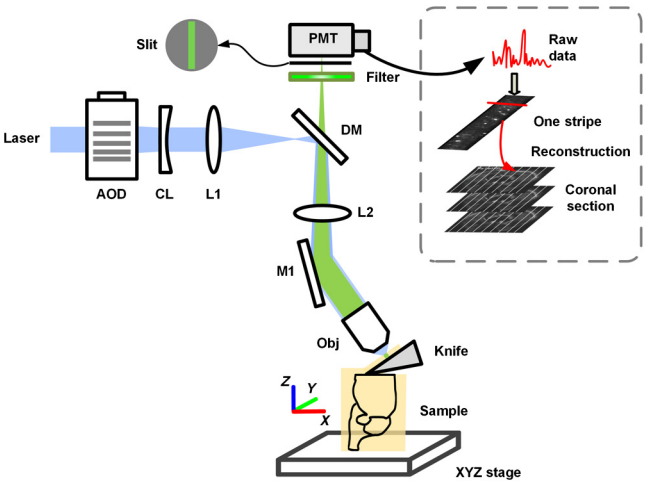

Fig. 1 System setup and imaging scheme of the confocal fluorescence micro-optical sectioning tomography (fMOST) system. A resin-embedded brain sample is mounted on a motorized XYZ stage. A diamond knife is used for slicing the embedded brain sample. Sliced sample strip adheres to and slides along the surface of the knife. Simultaneous scan imaging of the sliding sample strip is carried out with an acousto-optical deflector (AOD) scanner-based confocal microscope. Excitation laser is scanned along one direction by the AOD and passes through a cylindrical lens (CL), a scan lens (L1), a tube lens (L2), deflected by a mirror (M1) and focused by the objective lens to the sliding sample strip. Sample fluorescence is collected and passes through a dichroic mirror (DM), an emission filter, a custom-made confocal slit, and is detected by a photomultiplier tube. Raw data of one sample strip are constructed and stitched to one coronal section and three-dimensional (3-D) volumetric images can be reconstructed by stacking the images of each coronal section.

A mouse was anesthetized and sacrificed by transcardially fixative perfusion. The mouse brain was then postprocessed and resin-embedded. The embedded brain sample was mounted on the stage for image acquisition. The animal experiments were performed following procedures approved by the institutional animal ethics committee of Huazhong University of Science and Technology. Each time a strip (whose width is slightly smaller than the imaging field of view) was sliced and imaged, the sample was stepped in the y-direction and the adjacent sample strip was sliced and imaged. After all strips from a whole section had been imaged, the sample was stepped in the z-direction with a step size equal to the slicing thickness, and strip images from the next section were acquired by the aforementioned process. In this way, a complete image dataset of the whole brain can be acquired. Normally, a $0.5\times0.5\times2$ μm^3 voxel size was used for acquiring a whole mouse brain. Each scan line took about 200 μs, with a pixel dwell time of about 0.4 μs. The acquisition time for each coronal section of the mouse brain was close to 3 min. Images of ~5000 coronal sections were acquired for the whole mouse brain image dataset, which took about 250 h. High-precision sample slicing and imaging ensure that all strip images are naturally aligned, meaning that all the images can be easily stitched to give a well-aligned volume dataset. Imaging and sectioning control were realized by custom software based on LabVIEW.

3 Methods and Results

3.1 *Confocal Fluorescence Imaging over a Microtome Knife*

In the fMOST system, the sliced brain sample strips are imaged over the diamond knife. For a brain sample with fluorescently labeled neurons distributed across the whole brain, the brain samples under the diamond knife will also be excited (the diamond knife is not opaque to the excitation and emission light) and emit fluorescence. The fluorescence will appear as background noise in the sample strip image, and this noise should be suppressed to enhance the image contrast. For the imaging while sectioning method employed in the proposed system, the sample strips being imaged are sliced and separated from the sample under the knife, and the excitation light cone is elevated relative to the base of the sample, as illustrated in Fig. 2. This mechanical separation provides some degree of background suppression. A confocal scheme is employed to provide additional suppression of the fluorescence background. That is, we can tune the fluorescence background suppression by adjusting the optical sectioning capability (by changing the confocal slit width) or change the elevation distance of the excitation light cone by changing the imaging site over the diamond knife.

To further evaluate the effect of confocal detection and spatial separation (light cone elevation distance) on fluorescence background suppression, we constructed a simplified ideal

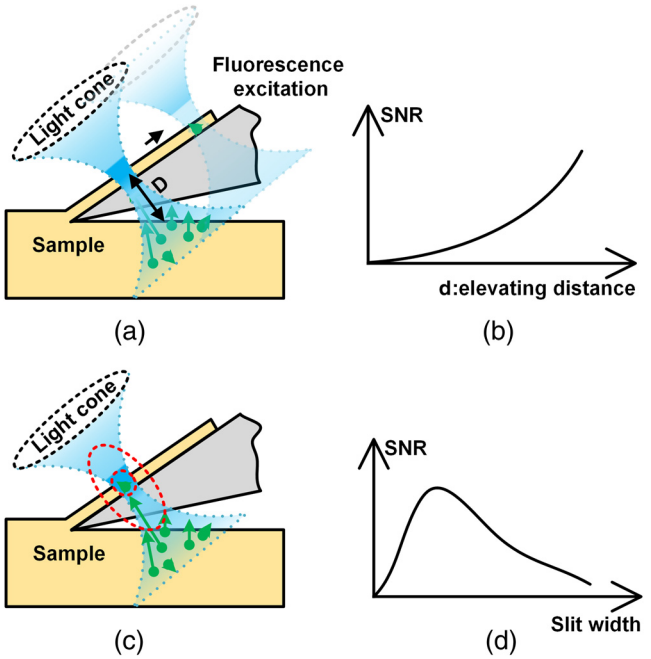

Fig. 2 Fluorescence excitation and emission in confocal fMOST system. (a) Light cone excites not only the sample strip over the knife but also the sample below, introducing background noise. There is a distance *D* between the sample strip and the bulk sample below. Moving the light cone along the knife increases the distance *D*, and the excited fluorescence background will decrease. (b) The signal-to-noise ratio (SNR) increases with *D*, as illustrated. (c) Using a confocal slit, the detection volume will be limited, and the fluorescence background will be reduced. (d) The relationship between SNR and slit width is illustrated.

model, as shown in Fig. 3, and considered an infinitely small pinhole for confocal detection analysis.

We use Born and Wolf analysis of the circular aperture diffraction problem[19,20] (modeling the objective lens). As shown in Fig. 3, the objective lens is simplified to a circular aperture of radius a with focal length z_f. The field at $P_d(x_d, y_d, z_d)$ near the focal point $P_f(0,0,z_f)$ of a spherical wave can be regarded as

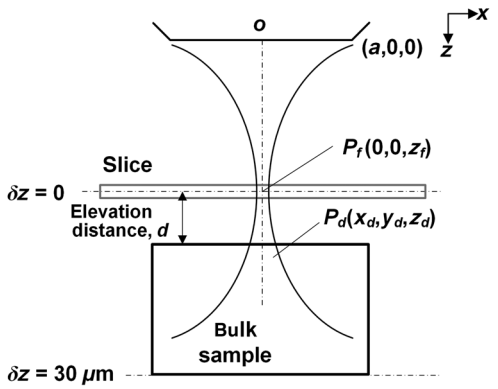

Fig. 3 Schematic diagram of a simplified imaging model. A 2-μm-thick slice is placed over the bulk sample with an elevation distance *d*. The objective lens is simplified as a circular aperture of radius *a* with a focal length of z_f. P_f is the focal point, P_d is a point near the focal point. By summing up the contribution from the points in the bulk sample, background intensity contribution from the bulk sample at different elevation distances can be analyzed. $\delta z = 0$ indicates the focal plane of the objective lens. The value of intensity point-spread function (PSF) at $\delta z > 30$ μm is very small and is neglected in the model.

the expression of the excitation point-spread function (PSF). In the objective lens, we use the approximation $\mathrm{NA} \approx a/z_f$. The complex amplitude at P_d is[21]

$$U[P_d(r,\delta z)] = \frac{kA}{iz_f} e^{ik\delta z} \int_0^1 J_0(kr\mathrm{NA}\rho) \times \exp\left(\frac{-ik\delta z \mathrm{NA}^2\rho^2}{2}\right)\rho \mathrm{d}\rho, \quad (1)$$

where A is the field amplitude on the optic axis of the aperture, $k = 2\pi/\lambda$, $\delta z = z_d - z_f$, $r = (x_d^2 + y_d^2)^{1/2}$, ρ is the radial coordinate with the optic axis as the center, and the cylindrical coordinate of each point in the aperture can be written as $(a\rho, \theta, 0)$, $0 \le \rho \le 1$.

The PSF at point P_d can be written as $h(P_d) = U(P_d)$. With the same objective lens used for both excitation illumination and emission detection, we can assume the illumination and detection PSF follow the same distribution function, ignoring the difference in wavelength. The imaging intensity PSF can be written as[21]

$$h = |h_{\mathrm{ex}}|^2[|h_{\mathrm{em}}|^2 * p_r(x,y)], \quad (2)$$

where $p_r(x,y)$ represents the aperture function of the pinhole of radius r, defined as

$$p_r(x,y) = \begin{cases} 1 & \text{if } \sqrt{x^2+y^2} \le r \\ 0 & \text{otherwise} \end{cases}. \quad (3)$$

For an infinitely small pinhole $p_r(x,y) = \delta(x,y)$, the PSF for the confocal condition can be simplified as

$$h = |h_{\mathrm{ex}}|^2|h_{\mathrm{em}}|^2. \quad (4)$$

As shown in Fig. 3, a 2-μm-thick slice is placed over the bulk sample with an elevation distance d. The PSF reflects the contribution of each point in the sample space to the detected intensity, assuming a uniform plane wave illumination parallel to the optic axis. The intensity PSF makes a negligible contribution when $r > 10$ μm or $\delta z > 30$ μm. Because the PSF is radially symmetric near the focal point, we consider only the xoz plane, and calculate the intensity PSF inside the regions defined by -10 $\mu\mathrm{m} \le x \le 10$ μm and 0 $\mu\mathrm{m} \le \delta z \le 30$ μm. The PSF is represented as a matrix $(a_{ij})_{301\times201}$, $i = 1,2,\ldots,301$; $j = 1,2,\ldots,201$. The elements of the matrix represent the intensity contribution from a 0.1 μm $\times$ 0.1 μm area of the detected signal.

The signal from a slice is calculated as $\sum_{1\le j\le 201}^{i=1} a_{ij} + 2\sum_{1\le j\le 201}^{2\le i\le 10} a_{ij}$, and the fluorescence background from the bulk sample can be calculated as $\sum_{1\le j\le 201}^{n+10<i\le 301} a_{ij}$, $n = d/0.1$. The SNR is defined as

$$\mathrm{SNR} = 10\cdot\log\left(\frac{\sum_{1\le j\le 201}^{i=1} a_{ij} + 2\sum_{1\le j\le 201}^{2\le i\le 10} a_{ij}}{\sum_{1\le j\le 201}^{n+10} a_{ij}}\right). \quad (5)$$

We first consider the nonconfocal condition, in which the confocal pinhole is not used. Figures 4(a)–4(c) show the background intensity from the bulk sample at various elevation distances ($d = 0$ μm, 5 μm, and 15 μm) summed along the z-axis. Figure 4(d) shows the signal intensity from the slice, summed along the z-axis. Figure 4(e) shows that SNR increases with elevation distance. The increase in SNR at different elevation

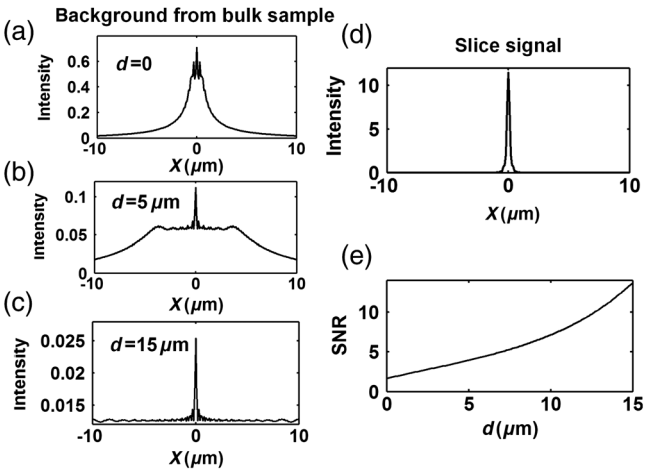

Fig. 4 Results for nonconfocal detection condition. (a, b, c) The background intensity contribution from the bulk sample (contribution along *x*-axis) at 0 μm, 5 μm, and 15 μm elevation distances. (d) The signal intensity from the sample slice (along *x*-axis). (e) SNR at different elevation distances *d*.

distances relative to the SNR at $d = 0$ has a hint of the background suppression effect of slice separation by mechanical sectioning. The SNR is about 1.6 at $d = 0$, and increases by a factor of 2.4, 4.3, and 8.3 at $d = 5$ μm, 10 μm, and 15 μm, respectively. In practice, the short pixel integration time at high imaging speeds requires high excitation power to enhance the signal intensity. This will generate a strong fluorescence background from the bulk sample beneath the diamond knife. The increase in SNR provided by physical separation alone does not provide sufficient suppression of the strong fluorescence background.

Figure 5 shows the results for the confocal condition when the detection pinhole is used. Figures 5(a)–5(c) show the background intensity from the bulk sample at increased elevation distances ($d = 0$ μm, 5 μm, and 15 μm) summed along the *z*-axis. Figure 5(d) shows the signal intensity from the slice summed along the *z*-axis. In Fig. 5(e), the SNR is about 79 at zero elevation. The SNR increases 52, 224, and 728 fold at 5 μm, 10 μm, and 15 μm elevation distances, respectively. The SNR increase

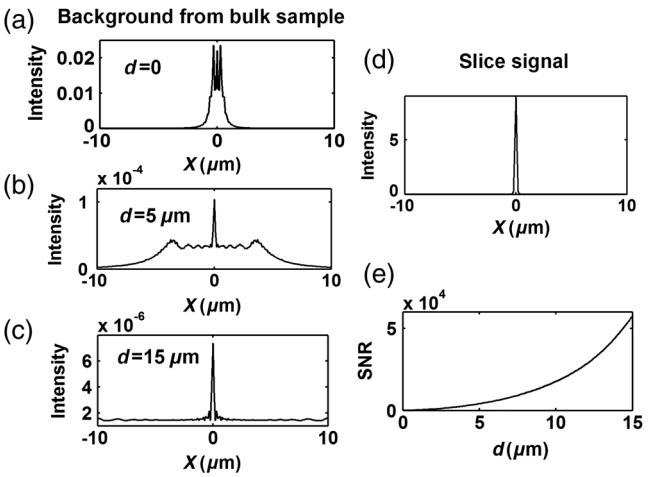

Fig. 5 Result for confocal detection condition. (a, b, c) The background intensity contribution from the bulk sample (contribution along *x*-axis) at 0 μm, 5 μm, and 15 μm elevation distances. (d) The signal intensity from the sample slice (along *x*-axis). (e) SNR at different elevation distances *d*.

resulting from the increase in elevation distance is much more obvious in the confocal condition than in the nonconfocal condition. Although this is a much simplified and idealized simulation, it suggests that, compared with normal confocal imaging, physical separation of the slice from the bulk sample below can greatly improve the suppression of fluorescence background, even with a small separation distance. Compared with the above results for the nonconfocal condition, the improvement in SNR with confocal detection is quite significant.

We illustrate the effect of combining confocal detection with physical separation on background suppression in Fig. 6. Resin-embedded mouse brain samples were used. Figures 6(a)–6(c) show the results from a thy1-GFP-M mouse brain sample. Figures 6(d)–6(f) show the result from a thy1-YFP-H mouse brain sample. For the experiments, a sample strip of thickness 2 μm containing a few fluorescent neurites was first sliced and collected. A confocal image of the sample strip was acquired using a Zeiss LSM 780 confocal microscope, with a $20\times/1.0$ objective lens and 50 μm pinhole diameter. Using the same imaging parameters as for the sample strip, confocal images of the remaining bulk sample block were then acquired with the objective focal plane set to 2 μm and 10 μm above the block surface, respectively. Figure 6 shows an overlay of these two images with the sample image. This can be regarded as a simulation of imaging with only the confocal scheme and imaging combining confocal detection with a small separation between the sample strip and the bulk sample. As seen in Figs. 6(a) and 6(d), residual fluorescence background from the cell body of neurons at the block surface can be visually identified. Intensity profile along the specified line [blue line in Figs. 6(a) and 6(d), and red line in Figs. 6(b) and 6(e)] shows that residual signal intensity from the cell body, which is located at the surface of the sample block, is close to or even larger than the signal from the neurites in the sample strip. Note that the fluorescence of the cell body can be several times brighter than that of the neurites. This accounts for the above fact that, even located at the defocused plane of a confocal microscope, the residual signal intensity from the cell body is still close to that from the neurites imaged at the focal plane. Figures 6(b) and 6(e) show that a 10 μm elevation of the focal plane (the light cone) largely suppresses the background. An image stack with the objective focal plane placed at the surface and above was also acquired and the residual signal from the cell body [indicated by the white arrow in Figs. 6(a) and 6(d)] at different elevation distances *d* are shown in the inset of Figs. 6(c) and 6(f). The normalized signal intensity drops from around 0.5 [0.44 and 0.57 respectively, in Figs. 6(c) and 6(f)] at $d = 2$ μm to around 0.1 at $d = 10$ μm [0.08 and 0.12 respectively, in Figs. 6(c) and 6(f)]. This demonstrates the necessity of combining confocal detection and physical separation for this type of neural wiring imaging application, where signal intensity from the cell body and that from the neurite can span an order of magnitude.

Confocal detection can also help to recover the signal from the small tears at the edge of adjacent strips that sometimes occur in the sectioning process.[22] The signal will otherwise be buried in the fluorescence background.

3.2 *Fast and Stable Scanning*

Fast and stable imaging is important for the acquisition of a complete whole-brain image dataset at submicron voxel size. For the point scan confocal imaging method, this requires a fast and stable scanner. As the time required to image a mouse brain

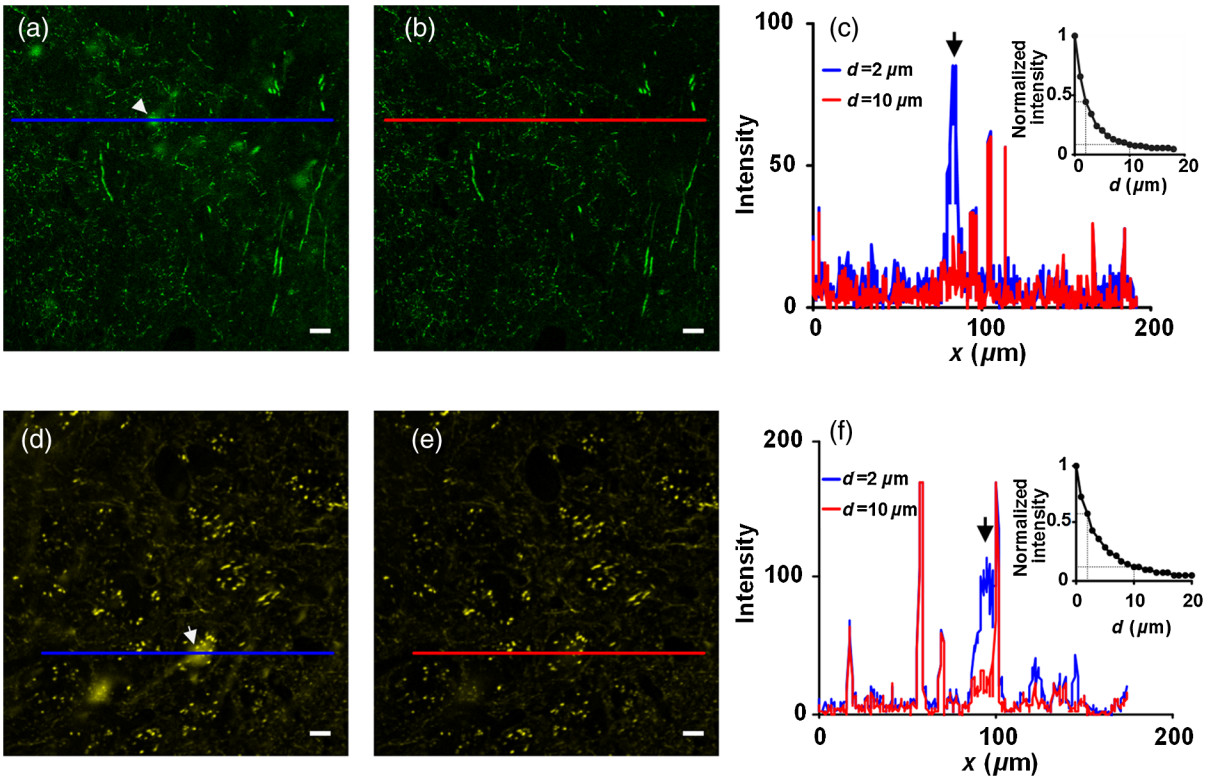

Fig. 6 Images given by overlaying confocal image of a sliced 2-μm-thick sample with a few fluorescent neurites inside and confocal image of the remaining bulk sample block with focal plane of the objective at a distance of 2 μm [(a, d)] and 10 μm [(b, e)] above block surface. Scale bar: 20 μm. Upper row shows the results from a thy1-GFP-M mouse brain and lower row shows the results from a thy1-YFP-H mouse brain. (c, f) The intensity profile along the specified lines in the images. (a, d) Black arrows indicate residual signal from cell bodies marked by the white arrows. (c, f) Inset plots show the residual signal from these two cell bodies at different elevation distances d of the objective focal plane.

could be more than 1 week with the point scan method, an inertia-free scanner based on the acousto-optical principle was chosen.[18,23]

The imaging of each sample strip requires the coordinated operation of the AOD scanner and the sample stage. AOD only produces a 1-D scan. For two-dimensional imaging, a scan along another dimension is given by sliding the sample strip over the knife (i.e., by moving the sample stage along the x-axis) (see Fig. 1).

To perform fast scanning, the AOD scanner works in a high-frequency chirp mode.[18,19] However, in this mode, the laser beam, in addition to being deflected, will also diverge or converge in only one direction, which will in turn cause astigmatism. Working in high-frequency chirp mode, the AOD is actually equivalent to a cylindrical acousto-optical lens (AO lens) with a focal length equal to $f = v^2/\lambda\alpha$,[24–26] where v is the propagation speed of an acoustic wave inside the AOD crystal, λ is the wavelength of the excitation light, and α is the rate of change of the acoustic frequency. The cause of astigmatism and its influence on imaging resolution are shown in Fig. 7. We can correct this effect by introducing a cylindrical lens (CL), which is placed after the AOD at a distance equal to the focal length difference of the AO lens and the introduced CL. The AOD used in our implementation has a frequency bandwidth of 50 MHz, and the scan time per line was set to 150 μs. The acoustic wave propagation speed is 650 m/s, and the calculated focal length of the AO lens is longer than 2 m. We made a custom CL with a focal length (absolute value) 30 mm shorter than that of the AO lens at 473 nm. With such long focal lengths of both the AO lens and the CL, we found that the distance between the two became less important, and can be fixed even at different excitation wavelengths (473/488 nm for GFP or 515 nm for YFP), although the resolution can be significantly improved, as shown in Fig. 8(b).

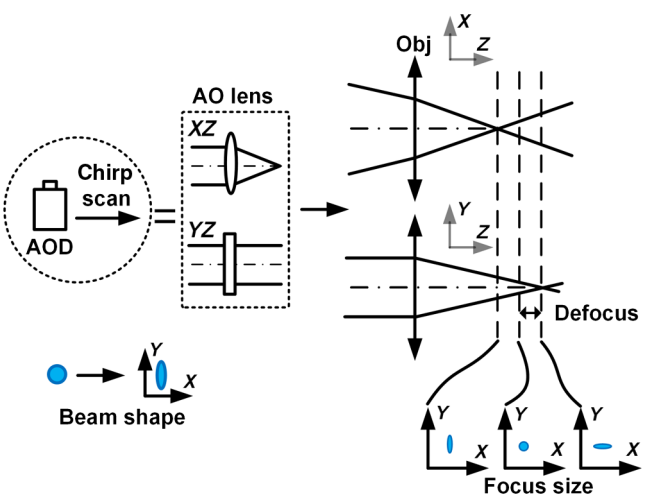

Fig. 7 Astigmatism caused by AOD working in the high-frequency chirp scan mode. In this mode, AOD is equivalent to a cylindrical lens (AO lens). Astigmatism occurs when the beam is focused by the objective lens.

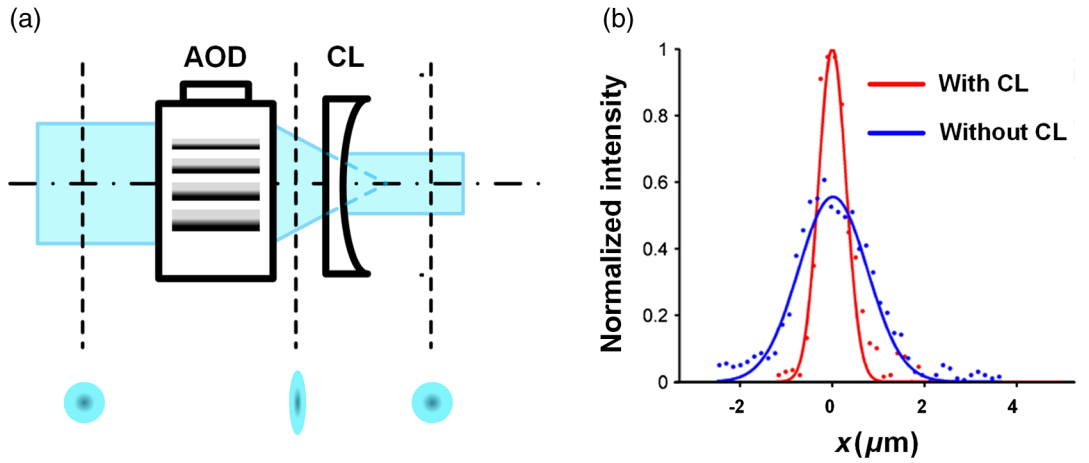

Fig. 8 A cylindrical lens can be introduced to correct the AOD astigmatism problem. (a) The CL was placed after the AOD. The distance between the two is equal to their focal length difference. (b) Spatial resolution and fluorescence intensity increased (~2 times) after the CL was introduced. Data from images of 170 nm fluorescent beads.

One disadvantage of AOD is the limited scan angle. We used a scan lens (L1 in Fig. 1) with a long focal length (400 mm), so that the scan angle at the back aperture of the objective lens will be 2.2 times that of the AOD. In this case, the beam diameter will also shrink. To make full use of the objective numerical aperture, we chose an AOD with a large aperture (15 mm), and maintained a 6.8 mm beam diameter at the back aperture of the objective lens. With the above configuration, a 375 μm scan length (488 nm excitation, 40× objective lens) can be achieved with submicron spatial resolution [Fig. 7(b), red line].

4 Conclusion and Discussion

We have developed an imaging system that combines confocal imaging and automatic mechanical sectioning for the acquisition of image datasets of large (centimeter-sized) samples. Both the mechanical separation of sample strips and the confocal detection scheme serve to improve the signal-to-background-noise ratio, and it is necessary to combine the two to achieve efficient background suppression. To enable long-term stability, an inertia-free AOD scanner with no possible mechanical wear was used. By working in a frequency chirped scan mode and correcting the accompanying astigmatism problem with a CL, a submicron lateral resolution can be maintained. To increase the scan angle and make full use of the aperture of the objective lens, a large aperture AOD was combined with beam shrinking.

We have presented a simplified simulation model to illustrate the effect of physical separation between the sample strips and confocal detection on the imaging SNR. In this simulation, we only considered the influence of the PSF of the excited fluorescence, and found that the SNR increases rapidly when the elevation distance of the excitation light cone is increased. In practice, SNR does not increase without limit with respect to the elevation distance. Instead, it will approach a constant. This is mainly due to autofluorescence noise and detector noise. Some other practical factors, e.g., the size of the confocal apertures, relationship between excitation light intensity and fluorescence intensity, aberrations introduced by the sample and knife, will also influence the system SNR.

Although increasing the light cone elevation distance by imaging the sample strip at a site far away from the knife blade will help to increase the SNR, there is one practical limitation. Good imaging quality requires the sample strip to be sectioned to maintain stable movement and adhere to the flat knife surface. This is only possible at points very close to the knife edge. In practice, the imaging site, i.e., the location of the scan line, must be adjusted to 5 to 15 μm from the knife edge, corresponding to an elevation distance of approximately 10 μm in the light cone.

To obtain a strong fluorescence signal from the thin sample strips at high imaging speed (i.e., short pixel integration times), high excitation power was used, which also increases the background fluorescence intensity from the bulk sample beneath, which may contain brightly labeled soma and densely innervated neurites. The proposed confocal scheme with physical separation for background suppression is, therefore, crucial for imaging quality.

As well as the combined optical and mechanical sectioning technique, there may be other possible solutions for the problem of background fluorescence. A diamond knife was used to maintain a thin and stable sectioning performance with the resin-embedded samples. This diamond knife is transparent to the excitation light and fluorescence. If a very-low-transmission coating could be applied to the surface of a diamond knife that can endure a long sectioning process, the fluorescence background would be greatly reduced. Another way to reduce the influence of background fluorescence is to use a special sample preparation technique to decrease or even quench the fluorescence from the sample area beneath the surface. This method would also enable the application of other optical imaging methods (widefield imaging, for example). We have explored some possible solutions[27] of this kind.

Acknowledgments

We thank Professor Duan Jun for manufacturing the confocal slit, and members of the Britton Chance Center for Biomedical Photonics for helpful discussions. This work was supported by the National Basic Research Program of China (Grant No. 2011CB910401), National High-tech R&D Program (Grant No. 2012AA020404), and National Natural Science Foundation of China (Grant Nos. 30925013, 61121004, and 2010DFR30820).

References

1. J. W. Lichtman and W. Denk, "The big and the small: challenges of imaging the brain's circuits," *Science* **334**(6056), 618–623 (2011).
2. J. DeFelipe, "From the connectome to the synaptome: an epic love story," *Science* **330**(6008), 1198–1201 (2010).
3. E. L. Bearer, X. Zhang, and R. E. Jacobs, "Live imaging of neuronal connections by magnetic resonance: robust transport in the hippocampal-septal memory circuit in a mouse model of Down syndrome," *NeuroImage* **37**(1), 230–242 (2007).
4. W. Denk and H. Horstmann, "Serial block-face scanning electron microscopy to reconstruct three-dimensional tissue nanostructure," *PLoS Biol.* **2**(11), e329 (2004).
5. J. A. Conchello and J. W. Lichtman, "Optical sectioning microscopy," *Nat. Methods* **2**(12), 920–931 (2005).
6. M. Oheim et al., "Two-photon microscopy in brain tissue: parameters influencing the imaging depth," *J. Neurosci. Methods* **111**(1), 29–37 (2001).
7. R. S. Fischer et al., "Microscopy in 3D: a biologist's toolbox," *Trends Cell Biol.* **21**(12), 682–691 (2011).
8. H. U. Dodt et al., "Ultramicroscopy: three-dimensional visualization of neuronal networks in the whole mouse brain," *Nat. Methods* **4**(4), 331–336 (2007).
9. K. D. Micheva and S. J. Smith, "Array tomography: a new tool for imaging the molecular architecture and ultrastructure of neural circuits," *Neuron* **55**(1), 25–36 (2007).
10. D. Mayerich, L. Abbott, and B. McCormick, "Knife-edge scanning microscopy for imaging and reconstruction of three-dimensional anatomical structures of the mouse brain," *J. Microsc.* **231**(1), 134–143 (2008).
11. A. Li et al., "Micro-optical sectioning tomography to obtain a high-resolution atlas of the mouse brain," *Science* **330**(6009), 1404–1408 (2010).
12. J. Livet, "The brain in color: transgenic 'Brainbow' mice for visualizing neuronal circuits," *Med. Sci.* **23**(12), 1173–1176 (2007).
13. J. Livet et al., "Transgenic strategies for combinatorial expression of fluorescent proteins in the nervous system," *Nature* **450**(7166), 56–62 (2007).
14. S. Gong et al., "A gene expression atlas of the central nervous system based on bacterial artificial chromosomes," *Nature* **425**(6961), 917–925 (2003).
15. C. Porrero et al., "Mapping of fluorescent protein-expressing neurons and axon pathways in adult and developing thy1-eYFP-H transgenic mice," *Brain Res.* **1345**, 59–72 (2010).
16. J. A. Harris, S. W. Oh, and H. Zeng, "Adeno-associated viral vectors for anterograde axonal tracing with fluorescent proteins in nontransgenic and cre driver mice," *Curr. Protoc. Neurosci.* **59**, 1–20 (2012).
17. K. Miyamichi et al., "Cortical representations of olfactory input by trans-synaptic tracing," *Nature* **472**(7342), 191–196 (2011).
18. H. Gong et al., "Continuously tracing brain-wide long-distance axonal projections in mice at a one-micron voxel resolution," *NeuroImage* **74**, 87–98 (2013).
19. M. Born and E. Wolf, *Principles of Optics*, Cambridge University Press, Cambridge, New York (1999).
20. S. F. Gibson and F. Lanni, "Diffraction by a circular aperture as a model for three-dimensional optical microscopy," *J. Opt. Soc. Am. A* **6**(9), 1357–1367 (1989).
21. F. Aguet, "Super-resolution fluorescence microscopy based on physical models," PhD Thesis, Swiss Federal Institute of Technology in Lausanne (2009).
22. X. Qi et al., "Improved detectability of neuronal connectivity on mechanical sectioning setup by using confocal detection," *J. Biomed. Opt.* **18**(5), 050506 (2013).
23. X. Qi, "Confocal fluorescence micro-optical sectioning tomography," PhD Thesis, Huazhong University of Science and Technology (2014).
24. G. D. Reddy and P. Saggau, "Fast three-dimensional laser scanning scheme using acousto-optic deflectors," *J. Biomed. Opt.* **10**(6), 064038 (2005).
25. A. Vanderlugt and A. M. Bardos, "Design relationships for acousto-optic scanning systems," *Appl. Opt.* **31**(20), 4058–4068 (1992).
26. A. Kaplan, N. Friedman, and N. Davidson, "Acousto-optic lens with very fast focus scanning," *Opt. Lett.* **26**(14), 1078–1080 (2001).
27. H. Xiong et al., "Chemical reactivation of quenched fluorescent protein molecules enables resin-embedded fluorescence microimaging," *Nat. Commun.* **5**, 3992 (2014).

Xiaoli Qi received her BS and PhD degrees in biomedical engineering in 2009 and 2014, respectively. Now, she is a postdoctoral fellow at the University of Washington. Her current research interest is optical coherence tomography and its physiological and clinical applications.

Tao Yang is a PhD student at Huazhong University of Science and Technology. He received his BS degree at Xidian University in 2010. He is developing a new imaging system for fast fluorescence imaging of the mouse brain.

Longhui Li is a PhD student at Huazhong University of Science and Technology. He received his BS degree at Huazhong University of Science and Technology in 2010. He is involved in developing the cooling system for the detector and the samples. He is also involved in developing the fast scan imaging system.

Jiancun Wang received his MS degree in biomedical engineering. He received his BS degree at Huazhong University of Science and Technology. He was involved in the image analysis, and the control system of the imaging setup.

Shaoqun Zeng is the deputy director of Wuhan National Laboratory for Optoelectronics, HUST. He received his PhD in physical electronics and optoelectronics in Huazhong University of Science and Technology. His research focuses on developing novel microscopic methods and their applications in neuroscience research.

Xiaohua Lv is an assistant professor at Wuhan National Laboratory for Optoelectronics, HUST. He received his BS and PhD degrees in biomedical engineering in 2002 and 2007, respectively. His research interests include fluorescence microscopy and optical recording and the application in neuroscience.